



Pyridinic nitrogen enriched porous carbon derived from bimetal organic frameworks for high capacity zinc ion hybrid capacitors with remarkable rate capability

Yao Li^a, Pengfei Lu^{b,e}, Ping Shang^a, Lisha Wu^a, Xiao Wang^{b,e}, Yanfeng Dong^{a,c,d,*}, Ronghuan He^a, Zhong-Shuai Wu^{b,e,*}

^a Department of Chemistry, College of Sciences, Northeastern University, Shenyang 110819, Liaoning, China

^b State Key Laboratory of Catalysis, Dalian Institute of Chemical Physics, Chinese Academy of Sciences, Dalian 116023, Liaoning, China

^c State Key Lab of Fine Chemicals, Dalian University of Technology, Dalian 116024, Liaoning, China

^d CAS Key Laboratory of Carbon Materials, Institute of Coal Chemistry, Chinese Academy of Sciences, Taiyuan 030001, Shanxi, China

^e Dalian National Laboratory for Clean Energy, Chinese Academy of Sciences, Dalian 116023, Liaoning, China

ARTICLE INFO

Article history:

Received 5 July 2020

Revised 29 July 2020

Accepted 8 August 2020

Available online 17 August 2020

Keywords:

Zinc ion hybrid capacitors

Nitrogen doping

Porous carbon

Metal organic frameworks

High capacity

ABSTRACT

Aqueous zinc ion hybrid capacitors (ZIHCs) hold great potential for large-scale energy storage applications owing to their high safety and low cost, but suffer from low capacity and energy density. Herein, pyridinic nitrogen enriched porous carbon (nPC) was successfully synthesized via the growth, subsequent annealing and acid etching of bimetal organic frameworks for high capacity and safe ZIHCs with exceptional rate capability. Benefiting from the mesopores for easy ion diffusion, high electrical conductivity enabled by in-situ grown carbon nanotubes matrix and residual metal Co nanoparticles for fast electron transfer, sufficient micropores and high N content (8.9 at%) with dominated pyridinic N (54%) for enhanced zinc ion storage, the resulting nPC cathodes for ZIHCs achieved high capacities of 302 and 137 mAh g⁻¹ at 1 and 18 A g⁻¹, outperforming most reported carbon based cathodes. Theoretical results further disclosed that pyridinic N possessed larger binding energy of -4.99 eV to chemically coordinate with Zn²⁺ than other N species. Moreover, quasi-solid-state ZIHCs with gelatin based gel electrolytes exhibited high energy density of 157.6 Wh kg⁻¹ at 0.69 kW kg⁻¹, high safety and mechanical flexibility to withstand mechanical deformation and drilling. This strategy of developing pyridinic nitrogen enriched porous carbon will pave a new avenue to construct safe ZIHCs with high energy densities.

© 2020 Science Press and Dalian Institute of Chemical Physics, Chinese Academy of Sciences. Published by ELSEVIER B.V. and Science Press. All rights reserved.

1. Introduction

Electrochemical energy storage devices (EESDs) could store intermittent and renewable energy resources (e.g., wind, solar) and provide electricity supply for energy consuming devices [1,2]. Recently, emerging aqueous zinc ion hybrid capacitors (ZIHCs) have attracted wide attention [3]. Typically, a ZIHC consists of a battery type zinc anode, mild aqueous electrolyte (e.g., 2 M ZnSO₄), and capacitive porous carbon cathode with fast physical adsorption/desorption mechanism. Therefore, ZIHCs possess

* Corresponding authors at: Department of Chemistry, College of Sciences, Northeastern University, Shenyang 110819, Liaoning, China (Y.F. Dong); State Key Laboratory of Catalysis, Dalian Institute of Chemical Physics, Chinese Academy of Sciences, Dalian 116023, Liaoning, China (Z.-S. Wu).

E-mail addresses: dongyanfeng@mail.neu.edu.cn (Y. Dong), wuzs@dicp.ac.cn (Z.-S. Wu).

advanced features of low cost, long service life, and high power density over zinc ion batteries with sluggish redox reaction mechanism [4–8]. Further, earth abundant and low cost metal zinc anode (\$65 kWh⁻¹ vs. \$300 kWh⁻¹ of metal Li) could deliver high theoretical capacity of 820 mAh g⁻¹, and the low redox potential of -0.76 V (vs. standard hydrogen electrode) guarantees outstanding compatibility in mild aqueous electrolytes with high ionic conductivity (~1 S cm⁻¹ vs. 0.01 S cm⁻¹ of organic electrolytes) [9–16], which could possibly address the issues of low power density and safety concern of lithium ion hybrid capacitors [17]. However, the fatal challenges of present ZIHCs are low capacity and inferior energy density of carbon cathodes [18–21], mainly limited by Zn²⁺ ion storage via physical adsorption/desorption mechanism.

To tackle these challenges, rational design of carbon materials with suitable porous structures could effectively provide more active sites for physical adsorption/desorption of Zn²⁺ for

improved performance of ZIHCS [18]. For instance, commercial activated carbon materials and graphene derived porous carbon with high specific surface area (SSA) ($>1923 \text{ m}^2 \text{ g}^{-1}$) were employed as superior carbon cathodes [19,20]. Notably, the presence of mesopore would greatly facilitate fast ion transport in carbon cathodes for high rate ZIHCS. As a typical example, phenolic resin derived hollow carbon spheres with rich mesopores (4.6 and 10.7 nm) delivered high capacities of 174.7 and 96.9 mAh g^{-1} at 0.1 and 10 A g^{-1} [21], respectively. Further, heteroatom doping could precisely adjust the band structures of carbon materials for enhanced conductivity, effectively tailor favorable surface chemistry for improved wettability in aqueous electrolyte, and importantly provide additional Zn^{2+} storage sites via chemical adsorption for enhanced zinc storage [22,23]. For example, N doped micro/mesoporous carbon exhibited higher capacity of 177.8 mAh g^{-1} at 4.2 A g^{-1} than undoped counterpart (67.8 mAh g^{-1}) [22]. And B/N co-doped carbon nanosheets were also demonstrated with superior zinc storage performance [23]. However, the capacities of most reported carbon cathodes are lower than 250 mAh g^{-1} [18–23], mainly owing to limited active sites and low heteroatom contents ($<8 \text{ at}\%$) for Zn^{2+} ion storage. Moreover, taking into the consideration of N doping types (e.g., pyridinic N, pyrrolic N), the optimal type with the underlying mechanism is still elusive. Therefore, rational construction of porous carbon with defined structure and targeted high N doped content is urgently required for developing high-performance ZIHCS.

Herein, we successfully synthesized pyridinic N enriched porous carbon (nPC) with high N content of 8.9 at% and micro/mesoporous structures mainly by Zn/Co bimetallic organic framework (ZnCoMOF) growth, subsequent annealing and acid etching processes for high-performance ZIHCS. The resulting nPC possessed several advantages in addressing the shortages of common carbon cathodes in ZIHCS: (i) The elaborate selection of ZnCoMOFs precursor ensured the co-existence of abundant micropores and mesopores for sufficient zinc storage sites and fast ion transport simultaneously [24]. (ii) High N doping level in nPC matrix, especially dominated pyridinic N (54%) with high binding energy with Zn^{2+} ions, provided additional active sites for improved zinc storage. (iii) The presence of in-situ grown carbon nanotubes (CNTs) and residual metal Co nanoparticles greatly facilitated fast electron transfer. As a result, the nPC based aqueous ZIHCS (nPC-aZIHCS) exhibited ultrahigh capacity of 302 mAh g^{-1} at 1 A g^{-1} , superior to most reported carbon cathodes. Moreover, nPC based quasi-solid-state ZIHCS (nPC-qZIHCS) delivered remarkable energy density of 157.6 Wh kg^{-1} with a power density of 0.69 kW kg^{-1} , and withstood mechanical deformation and drilling test, demonstrative of excellent flexibility and high safety.

2. Experimental

2.1. Materials synthesis

Preparation of ZnCoMOFs: The ZnCoMOFs were synthesized according to the reported work [25]. Typically, 120 mL of 2-methylimidazole ($\text{C}_4\text{H}_6\text{N}_2$, 7.88 g) aqueous solution was firstly poured into 120 mL of mixed solution with $\text{Zn}(\text{NO}_3)_2 \cdot 6\text{H}_2\text{O}$ (1.77 g) and $\text{Co}(\text{NO}_3)_2 \cdot 6\text{H}_2\text{O}$ (1.73 g). Then, the reaction of the ZnCoMOFs growth was kept for 4 h under magnetic stirring. After that, the centrifugation and washing with water for 3 times were conducted to remove unreacted species. Lastly, purple ZnCoMOFs powder was collected after vacuum drying at 100 °C for 10 h. For comparison, Zn based MOFs (ZnMOFs) were also prepared via the similar processes to the ZnCoMOFs, in which only $\text{Zn}(\text{NO}_3)_2 \cdot 6\text{H}_2\text{O}$ (3.54 g) was employed as metal precursor instead of zinc nitrate and cobalt nitrate.

Preparation of nPC: The ZnCoMOFs were annealed at 750 °C for 1 h in Ar, and the resulting sample was subsequently etched in dilute HCl (0.1 mol L^{-1}) for 12 h to eliminate most metal species. After that, the solution was centrifuged and washed by H_2O until the pH value approached to 7. Finally, the nPC powder was harvested after vacuum drying at 100 °C for 12 h. For comparison, ZnCoMOFs were annealed at 600 °C and 900 °C, and the corresponding final samples were denoted as nPC-600 and nPC-900, respectively. Moreover, N doped microporous carbon (mPC) was prepared by a similar experimental procedure of nPC except for the use of ZnMOFs instead of ZnCoMOFs.

Preparation of gelatin based quasi-solid-state electrolytes: gelatin (3 g) was dissolved in ZnSO_4 solution (12 mL, 1 M) at 60 °C [26]. Afterwards, the mixed solution was transferred into a homemade mold and kept at $-4 \text{ }^\circ\text{C}$ in a refrigerator for 12 h. Finally, quasi-solid-state electrolyte films with a typical thickness of 600 μm were obtained and cut into pieces with desirable sizes for subsequent nPC-qZIHCS assembly.

2.2. Characterization

The structure and chemical composition of nPC were measured with scanning electron microscope (SEM, SU8000), transmission electron microscope (TEM, JEM-2100), X-ray diffraction patterns (XRD, PANalytical Empyrean), nitrogen adsorption and desorption testing (a Quadrasorb SI analyzer), Raman spectroscopy (Xplora), and X-ray photoelectron spectroscopy (XPS, AXIS Ultra DLD).

2.3. Electrochemical measurement

The cathodes consisted of nPC (70 wt%), carbon black (20 wt%), and polyvinylidene fluoride (10 wt%) on carbon cloth (12 mm in diameter), in which the areal mass loading of nPC was about 1.1 mg cm^{-2} . Commercial zinc foils were directly employed as anodes. Aqueous and quasi-solid-state ZIHCS were assembled with 2M ZnSO_4 and gelatin based quasi-solid-state electrolyte, respectively. Galvanostatic charge/discharge (GCD) curves were performed with a battery system (LAND CT2001A). Cyclic voltammetry (CV) curves and electrochemical impedance spectroscopy (EIS) were tested with a CHI 660E workstation, specifically, an AC amplitude of 5 mV and the frequency from 100 kHz to 0.01 Hz were applied for EIS measurement. The energy density (E) and power density (P) of ZIHCS were calculated based on the mass (m) of nPC via two equations of $E = \int I V dt / 3.6m$ and $P = 3600E/t$, in which I , V and t represented the discharge current, the voltage after ohmic drop and discharge time [23,27], respectively.

2.4. Theoretical simulation

Theoretical simulation was conducted with CASTEP code combined with Materials Studio 6.0 package. The various models of perfect graphene (G), graphene modified with micropore (mG), graphitic nitrogen (GN), pyridinic nitrogen (PdN), and pyrrolic nitrogen (PrN) were established to investigate their binding energies (E) with Zn^{2+} . The energies of Zn^{2+} and each model system were denoted as E_{Zn} and E_{m} , respectively, and the energy of the investigated model with an adsorbed Zn^{2+} was E_{abs} , therefore, the binding energy between Zn^{2+} and the investigated model could be calculated via the equation of $E = E_{\text{Zn}} + E_{\text{m}} - E_{\text{abs}}$.

3. Results and discussion

The fabrication procedure of nPC mainly included ZnCoMOF growth, subsequent annealing and acid etching process, as shown

in Fig. 1. During the growth of ZnCoMOFs, Zn and Co metal ions acting as knots were coordinated with organic ligands of 2-methylimidazole, forming the frameworks with abundant cavities [28]. The facile synthesis and unique structure of ZnCoMOFs make them as versatile precursors for advanced electrodes in energy applications [29,30]. The ZnCoMOFs showed leaf-like morphology with a typical length of 10.8 μm and thickness of 450 nm (Fig. 2a). Subsequently, ZnCoMOFs were annealed at high temperature (600, 750, and 900 $^{\circ}\text{C}$) in Ar atmosphere to form nitrogen doped carbon, and the in-situ generated metal Zn was partly vaporized from the carbon matrix to generate abundant micropores [31–34]. Notably, in-situ generated Co nanoparticles could catalytically grow CNTs and graphitic carbon shells simultaneously (Figs. 2b and S1) [35]. In contrast, no CNTs were found in the case of ZnMOFs derived mPC and nPC-600 (Fig. S2). Further, clear lattice fringes of graphitic layers were observed in high-resolution TEM (HRTEM) image (Fig. 2c), and the expanded interlayer spacings of 0.37 and 0.38 nm were labeled by yellow arrows in different zones, which were attributed to the N doping effects in the carbon matrix [36]. Further, some residual Co nanoparticles were survived from acid etching process due to the protection of graphitic shells, and the (111) lattice plane of Co (JCPDS no. 15-0806) with the interlayer spacing of 0.2 nm was indicated in Fig. 2(c). Moreover, elemental mapping analysis validated the distribution of C and N in the corresponding zone of nPC, and the presence of element Co corresponding to Co nanoparticles in nPC (Fig. 2d). Importantly, abundant micro/mesopores in nPC were created after removing most Zn/Co based species by HCl etching.

Furthermore, the structures and chemical components of nPC were systematically characterized. As shown in Fig. 3(a), XRD pattern showed only one broad peak appeared in the range of 21° – 29° for ZnMOF derived mPC [31]. While in the case of ZnCoMOF derived nPC, two peaks at 23.2° and 25.7° were combined to form a similar broad peak to mPC, which was consistent with different interlayer spacings of 0.35 and 0.38 nm in the HRTEM analysis (Fig. 2c). The expanded interlayer spacing was ascribed to high N doping [37]. Moreover, a prominent peak at 44.2° and a weak one at 51.5° were assigned to the (111) and (200) signals of Co (JCPDS. no 15-0806) [38], indicating the existence of residual Co species. Further, N_2 adsorption and desorption measurement was conducted to investigate the porous structures of nPC and mPC (Fig. 3b and c), in which the SSA of $437\text{ m}^2\text{ g}^{-1}$ and the presence of micropore ($\sim 1.1\text{ nm}$) and mesopore (3.4 nm) were recorded for nPC, while higher SSA of $793\text{ m}^2\text{ g}^{-1}$ was achieved for mPC. However, the mesoporous volume of mPC ($0.065\text{ cm}^3\text{ g}^{-1}$) was much lower than that of nPC ($0.085\text{ cm}^3\text{ g}^{-1}$). Therefore, the elab-

orate selection of ZnCoMOFs precursor would provide a versatile platform to create abundant micropores and mesopores in nPC [39]. Moreover, both nPC and mPC showed two prominent signals at $\sim 1340\text{ cm}^{-1}$ (D band) and 1597 cm^{-1} (G band) [40]. However, nPC possessed a slightly lower ratio of D and G peak intensity (I_D/I_G) (0.83) than mPC (0.86) (Fig. 3d), suggesting the higher degree of graphitization in nPC due to the catalytic effect of Co for the formation of graphitic carbon. Additionally, high N content of 8.9 at% was measured by XPS analysis (Fig. 3e and f), and the N 1s spectrum could be deconvoluted into PdN at 398.7 eV, PrN at 400.3 eV, and GN at 401.3 eV [24,37], and their percentages were calculated to be about 54%, 29% and 17%, respectively, indicative of PrN enriched carbon. Notably, the percentage of PrN could be well controlled in the range of 44%–56% by changing annealing temperature of ZnCoMOFs (Fig. 3f and S3).

To demonstrate the advantageous features of as-fabricated nPC with abundant micro/mesopores and high N content, nPC-aZIHCS in coin cells were assembled with Zn foil anode and 2M ZnSO_4 electrolyte (Fig. 4a), and tested within 0.15–1.7 V vs. Zn^{2+}/Zn (Fig. 4b). It can be seen that the nPC-aZIHCS exhibited high discharge and charge capacities of 435 and 302 mAh g^{-1} at 1 A g^{-1} for the 1st cycle, in which a short discharge voltage plateau between 0.5 and 0.7 V was observed, resulting from zinc ion intercalation [41]. In the 2nd discharge profile, a remarkable capacity of 291 mAh g^{-1} was achieved without obvious plateaus, due to the dominated physical absorption of zinc ions mechanism. Therefore, high value of 243 mAh g^{-1} and good Coulombic efficiency of $\sim 100\%$ were maintained for nPC cathode after 80 cycles (Fig. 4c). It is noted that, although nPC and nPC-600 possessed similar N doping values, nPC-600 exhibited inferior conductivity with higher charge transfer resistance (Fig. S4). While nPC-900 possessed a low N doping value of 3.8 at%, therefore, nPC-600 and nPC-900 cathodes only delivered 209 and 202 mAh g^{-1} at 80th cycle (Fig. 4c). The superiority of nPC over nPC-600 also resulted in the improved reversibility of Zn anodes (Figs. S5). Moreover, mPC cathode showed enhanced zinc storage performance in comparison with mPC-600 (Fig. 4d and S6), demonstrative of the key role of carbonization temperature in the optimization of performance. Even at 5 A g^{-1} , nPC still showed high capacities of 195 and 204 mAh g^{-1} for 2nd and 10000th cycles, indicating the superior cycling stability (Fig. 4d). However, mPC cathode only exhibited 177 mAh g^{-1} with a low capacity retention of 83% after 10,000 cycles (Fig. 4d). Further, GCD profiles recorded at 1, 3, 5, 10 and 18 A g^{-1} exhibited similar electrochemical behaviors, and the corresponding capacities were 304 mAh g^{-1} (2nd cycle), 217 mAh g^{-1} (12th cycle), 193 mAh g^{-1} (22th cycle), 162 mAh g^{-1} (32th cycle), and 137

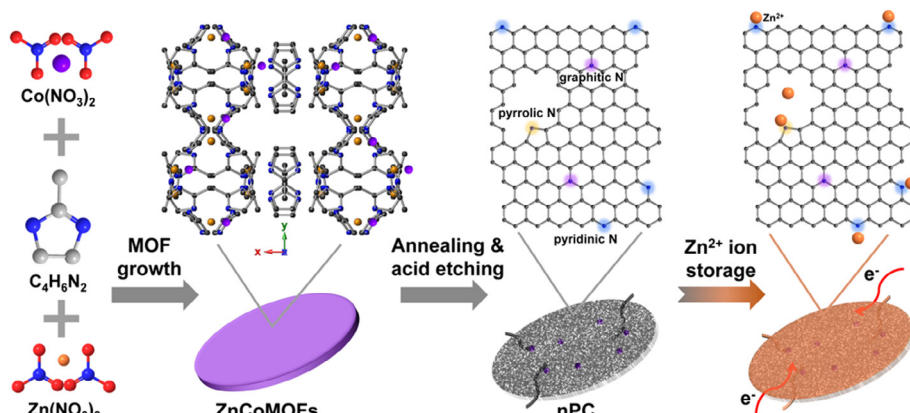


Fig. 1. Schematic of the preparation of the nPC cathode for zinc ion storage in ZIHCS, including MOF growth, annealing treatment of as-prepared ZnCoMOFs and acid etching of metal species.

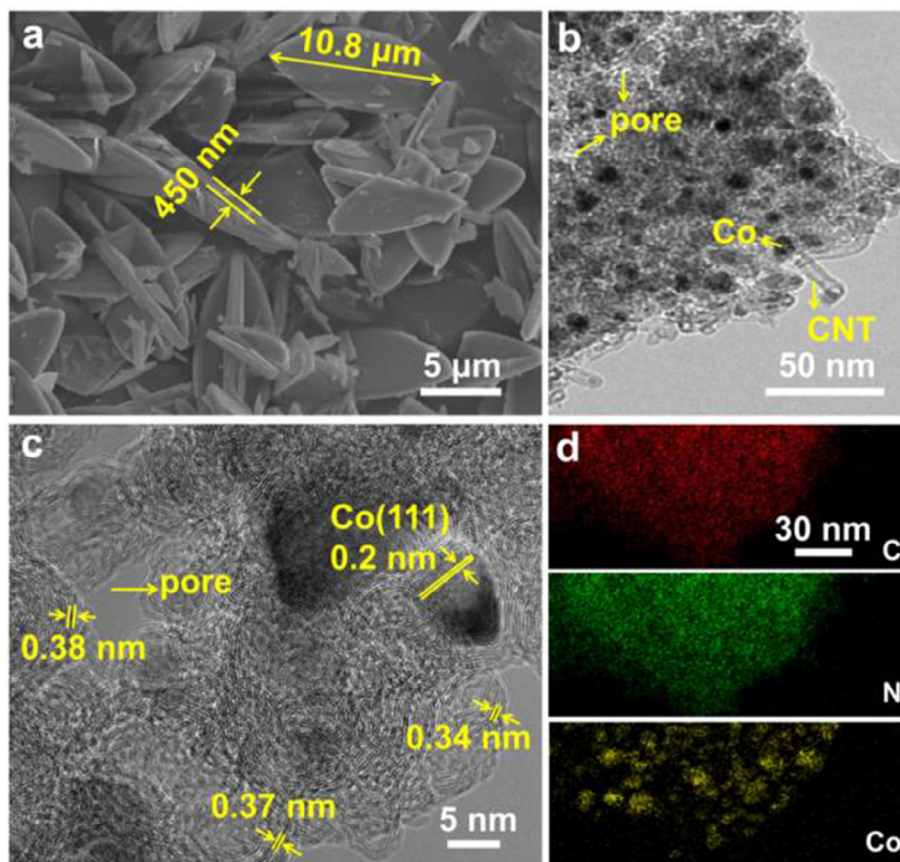


Fig. 2. (a) SEM image of ZnCoMOFs. (b) TEM and (c) HRTEM images of nPC. (d) Elemental mapping analysis of C, N and Co in nPC.

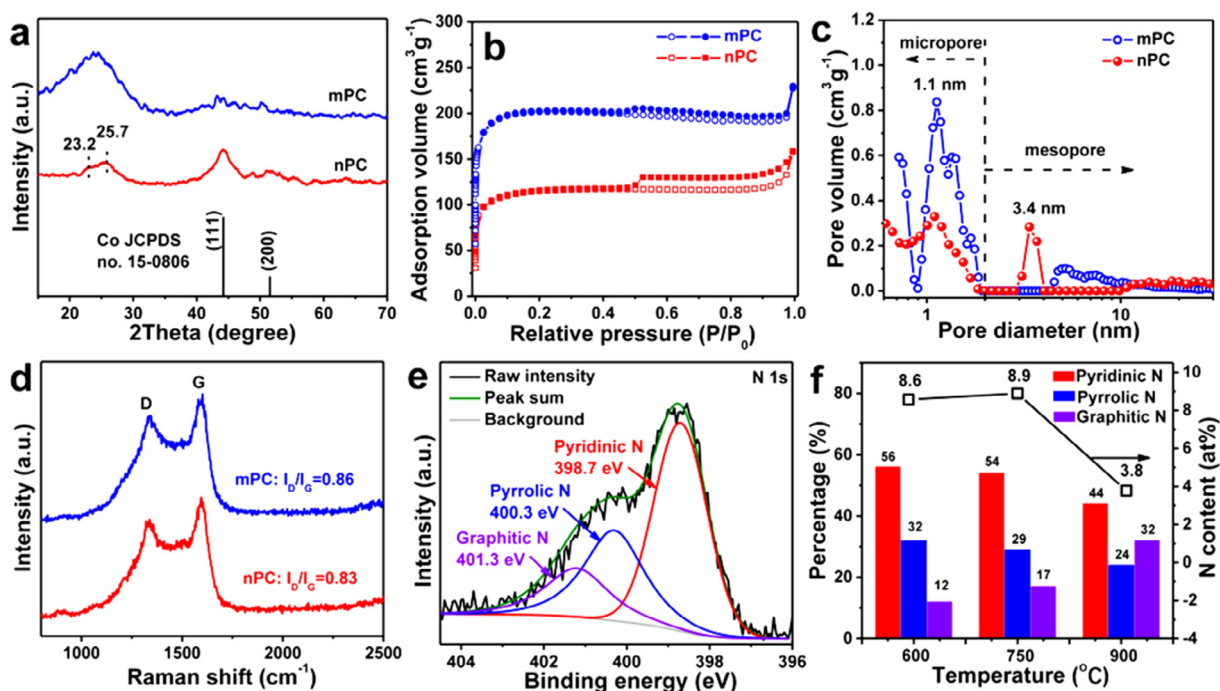


Fig. 3. (a) XRD patterns of nPC and mPC. (b) The N_2 adsorption and desorption isotherms and (c) pore size distributions of nPC and mPC. (d) Raman spectra of nPC and mPC. (e) N 1s XPS spectrum of nPC. (f) N contents and percentages of different N types in nPC products obtained at 600, 750 and 900 °C.

mAh g^{-1} (42th cycle) (Fig. 4e and f), respectively. Clearly, these results outperform the values of mPC (e.g., 103 mAh g^{-1} at 18 A

g^{-1}) (Fig. S7), and reported carbon cathodes (Fig. 4g), such as pencil shaving derived porous carbon (141 mAh g^{-1} at 1 A g^{-1}) [42],

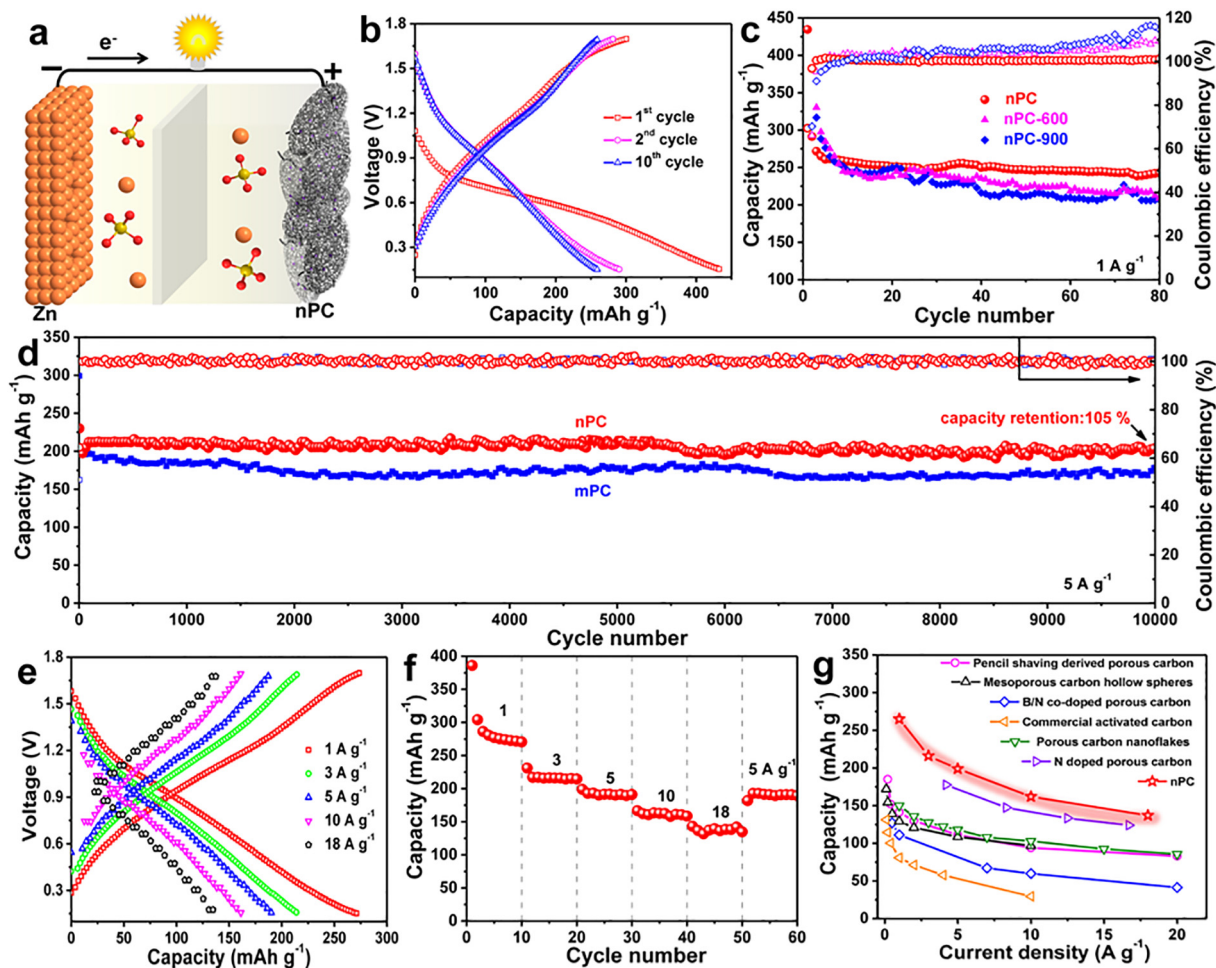


Fig. 4. Electrochemical performance of nPC-aZIHs. (a) Schematic illustration of a nPC-aZIHs. (b) GCD profiles of nPC-aZIHs obtained at the 1st, 2nd and 10th cycles. (c) Cycling stability and Coulombic efficiencies of the nPC, nPC-600 and nPC-900 electrodes for ZIHs. (d) Long cycling performance of the nPC and mPC cathodes at 5 A g⁻¹. (e) GCD profiles and (f) rate capability of nPC-aZIHs measured at various current densities of 1, 3, 5, 10, 18 A g⁻¹. (g) Comparison of zinc storage capacities of the nPC cathode for ZIHs with reported carbon based electrodes.

mesoporous carbon hollow spheres (130 mA h g⁻¹ at 1 A g⁻¹) [21], B/N co-doped porous carbon (111 mA h g⁻¹ at 1 A g⁻¹) [23], commercial activated carbon (81 mA h g⁻¹ at 1 A g⁻¹) [43], porous carbon nanoflakes (150 mA h g⁻¹ at 1 A g⁻¹) [44], and N doped porous carbon (178 mA h g⁻¹ at 4 A g⁻¹) [22].

To illustrate the electrochemical reaction kinetics of nPC-aZIHs, CV curves were further examined at scan rates from 3 to 50 mV s⁻¹ (Fig. 5a), in which the reversible reduction peak (Peak R) and oxidation peak (Peak O) were observed. The shape of CV curves indicated the integration of diffusion and capacitive processes in nPC cathodes [42]. To quantify the capacitive contribution, the peak current (*i*) and scan rate (*v*) were analyzed via $\log(i) = b\log(v) + \log(a)$ [45,46], in which *a* and *b* ($0.5 < b < 1$) are adjustable constants, and the *b_O* and *b_R* values of peak O and R were fitted to be 0.85 and 0.86 (Fig. 5b). Notably, the values of capacitive contribution increased from 44.7% at 3 mV s⁻¹ to 78.6% at 50 mV s⁻¹ (Figs. 5c, d and S8), suggesting the dominated capacitive mechanism at high rates [42,47].

To better understand the superior zinc storage performance of nPC, density functional theory (DFT) calculations were conducted. Pure graphene (G) (Figs. 6a and S9a), microporous graphene (mG) with an in-plane pore diameter of ~1.4 nm (Figs. 6b and S9b), GN doped graphene (Figs. 6c and S9c), PrN doped graphene (Figs. 6d and S9d) and PdN doped graphene (Figs. 6e and S9e) were selected as investigated models to study their interactions with Zn²⁺ ions. In

the case of mG, Zn²⁺ ion could be physically adsorbed in the micropore with a moderate binding energy of -3.66 eV (Figs. 6f and S10). And negligible binding energies of -0.14 and -0.16 eV were calculated for both G and GN due to their low electron donating abilities, suggesting that Zn²⁺ ions were hardly stored in these sites. Surprisingly, high binding energies of -4.99 eV and -4.63 eV were recorded for PdN and PrN (Figs. 6f and S10), respectively, due to their abilities to donate electrons to the unoccupied *d* orbital of Zn²⁺ ions [48]. Importantly, PdN was identified to greatly facilitate zinc storage via chemical coordination, unveiling the underlying mechanism of PdN enriched nPC with moderate SSA for ultrahigh capacities.

The excellent zinc storage performance of nPC-aZIHs motivated us to further construct flexible and safe quasi-solid-state ZIHs. To this end, environmentally friendly gelatin and low cost ZnSO₄ were employed to fabricate quasi-solid-state electrolyte films [26], which were directly employed as electrolyte and separator to assemble nPC-qZIHs (Fig. 7a). nPC-qZIHs exhibited similar electrochemical behavior to nPC-aZIHs in the initial two cycles. Specifically, nPC-qZIHs exhibited a discharge capacity of 522 mA h g⁻¹ at 1 A g⁻¹ for the 1st cycle, and a reversible capacity of 291 mA h g⁻¹ for the 2nd cycle (Fig. 7b and c). Further, the excellent cycling stability was confirmed by the low capacity fading rate of 0.125 mA h g⁻¹ per cycle over 1000 cycles, which could be reproducible at current density of 5 A g⁻¹ (Fig. 7b). Moreover, nPC-

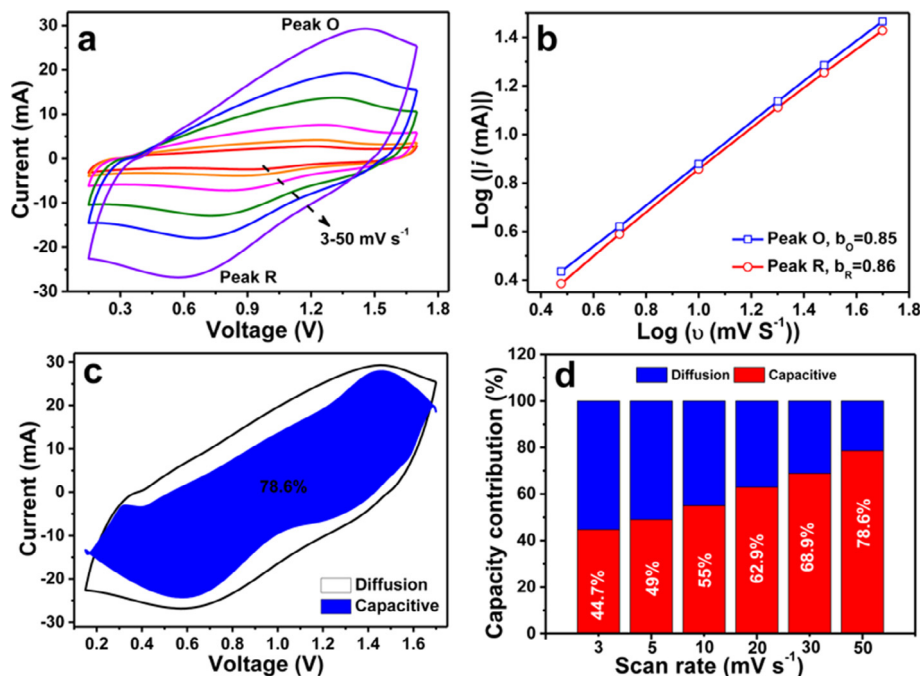


Fig. 5. Electrochemical kinetics analysis of nPC-aZIHs. (a) CV curves of nPC-aZIHs measured at different scan rates from 3 to 50 mV s^{-1} , and (b) the plots of corresponding $\log i$ versus $\log v$ curves of peak O and Peak R. (c) Diffusion and capacitive contribution at 50 mV s^{-1} . (d) Normalized capacity contributions at different scan rates from 3 to 50 mV s^{-1} .

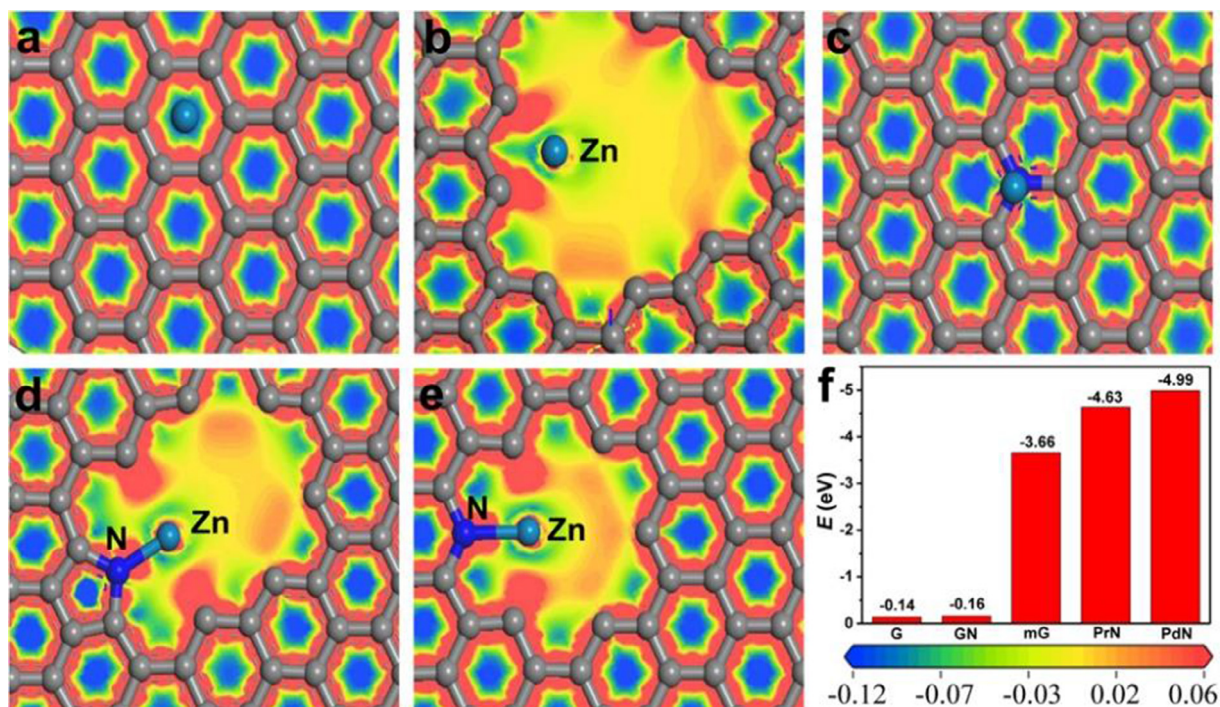


Fig. 6. The electron density distributions of (a) graphene (G), (b) holey graphene with a micropore (mG), (c) GN doped graphene, (d) PrN doped graphene, and (e) PdN doped graphene, in which a Zn^{2+} ion was absorbed on each model. (f) The comparison of binding energies between a Zn^{2+} ion and various models in (a–e).

qZIHs were evaluated at various current densities of 1, 3, 5, 10 and 18 A g^{-1} , and corresponding capacities of 259 mAh g^{-1} (2nd cycle), 164 mAh g^{-1} (12th cycle), 123 mAh g^{-1} (22th cycle), 74 mAh g^{-1} (32th cycle), and 28 mAh g^{-1} (42th cycle) were achieved (Fig. 7d), respectively. Notably, maximum energy densities of 157.6 and 203.1 Wh kg^{-1} (based on the mass of nPC) were achieved for

nPC-qZIHs and nPC-aZIHs, respectively. The energy densities of both nPC-aZIHs and nPC-qZIHs outperformed most cathodes in ZIHs (Fig. 7e and Table S1), such as mesoporous carbon hollow spheres (190 Wh kg^{-1}) [21], graphene derived porous carbon (aMEGO) (99.2 Wh kg^{-1}) [20], porous carbon nanoflakes (34.5 Wh kg^{-1}) [44], N doped porous carbon (87.5 Wh kg^{-1}) in solid-

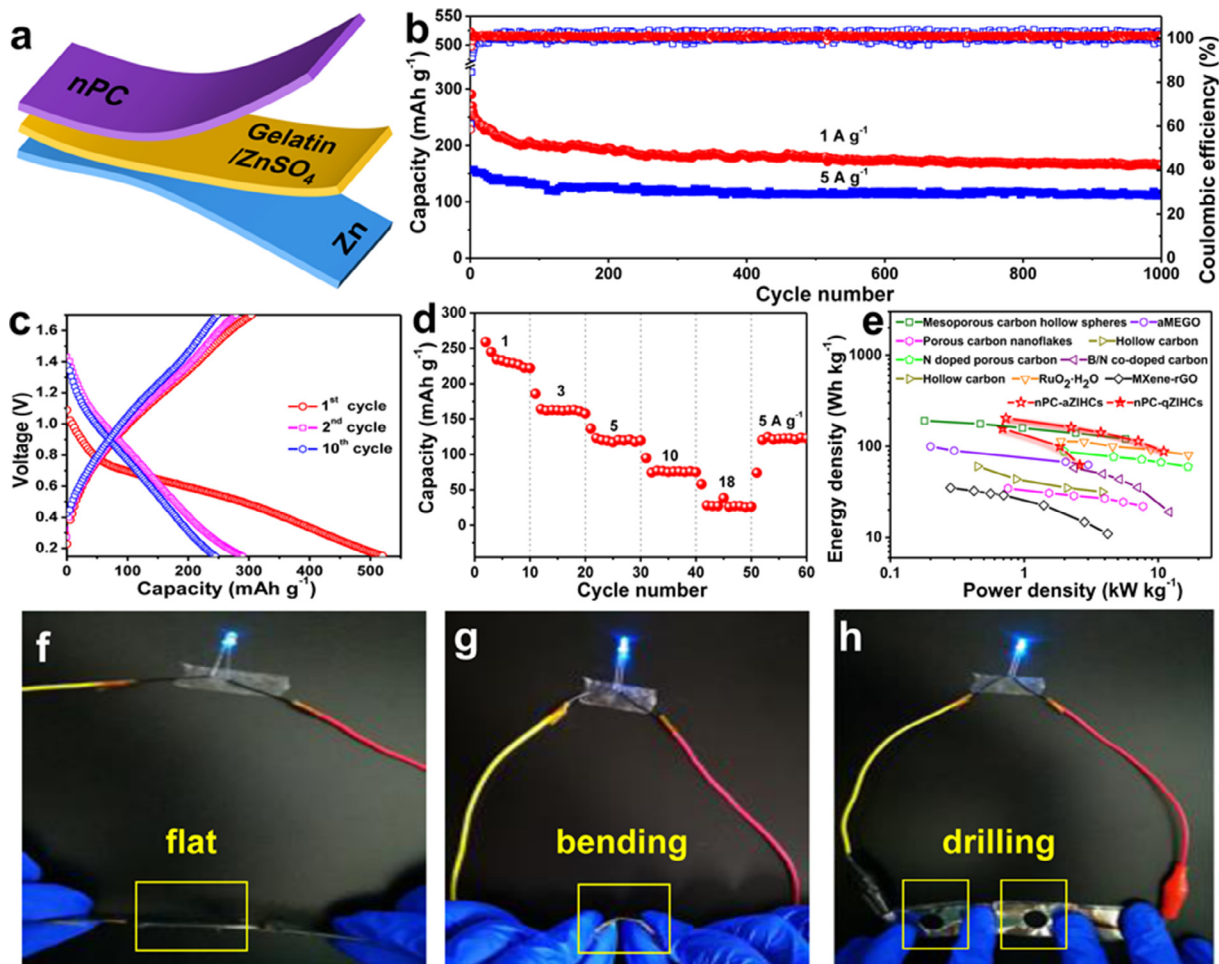


Fig. 7. Electrochemical performance of nPC-qZHCs. (a) Schematic illustration of nPC-qZHCs. (b) Cycling stability and Coulombic efficiency of the nPC-qZHCs at 1 and 5 A g⁻¹. (c) GCD profiles of the nPC-qZHCs obtained at the 1st, 2nd and 10th cycles at 1 A g⁻¹. (d) Rate capability of the nPC-qZHCs, measured at current densities of 1, 3, 5, 10, 18 A g⁻¹. (e) Ragone plots of nPC-aZHCs and nPC-qZHCs compared with reported carbon cathodes in ZHCs. Two soft-packaged nPC-qZHCs devices could light up a small bulb under (f) flat state, (g) bending state and (h) drilling state.

state ZHCs [22], B/N co-doped carbon (57.93 Wh kg⁻¹) [23], hollow carbon (60.13 Wh kg⁻¹) [18], RuO₂-H₂O (113.7 Wh kg⁻¹) [49], and MXene-rGO (35.03 Wh kg⁻¹) [50]. Importantly, two soft-packaged nPC-qZHCs connected in series could successfully light a LED bulb (Fig. 7f), and the brightness of the bulb was not affected even in bending and drilling test (Fig. 7g and h), demonstrating the flexibility and high safety of nPC-qZHCs.

4. Conclusions

In summary, we reported the efficient synthesis of bimetal organic frameworks derived nPC for high capacity and high rate ZHCs. The nPC was configured with micro/mesopores for physical adsorption/desorption of Zn²⁺ and fast ion transport, and abundant N active sites for additional Zn²⁺ storage. Theoretical results further confirmed that pyridinic nitrogen possessed higher binding energy with Zn²⁺ ions than other N species. As a result, the nPC cathodes in aqueous ZHCs exhibited excellent zinc storage, such as high reversible capacity of 302 mAh g⁻¹ at 1 A g⁻¹ and long service life of 10,000 cycles. Further, nPC-qZHCs exhibited high energy density of 157.6 Wh kg⁻¹. And most importantly, the soft-packaged ZHCs showed high safety and flexibility to withstand mechanical bending and drilling without sacrificing the performance. Therefore, this work will shed new light on zinc storage mechanism and elaborated construction of high energy density ZHCs.

Declaration of Competing Interest

The authors declare that they have no known competing financial interests or personal relationships that could have appeared to influence the work reported in this paper.

Acknowledgments

This work was financially supported by the National Key R&D Program of China (Grants 2016YBF0100100 and 2016YFA0200200), National Natural Science Foundation of China (Grants 51872283, and 21805273), Liaoning BaiQianWan Talents Program, Liaoning Revitalization Talents Program (Grant XLYC1807153), Natural Science Foundation of Liaoning Province (2020-MS-095), Joint Research Fund Liaoning-Shenyang National Laboratory for Materials Science (Grants 20180510038), DICP (DICP ZZBS201708, DICP ZZBS201802, and DICP I202032), DICP&QIBEBT (Grant No. DICP&QIBEBT UN201702), Dalian National Laboratory For Clean Energy (DNL), CAS, DNL Cooperation Fund, CAS (DNL180310, DNL180308, DNL201912, and DNL201915), the Fundamental Research Funds for the Central Universities of China (N180503012), the State Key Laboratory of Fine Chemicals (KF1911), and the CAS Key Laboratory of Carbon Materials (KLCMKFJJ2004). Special thanks are due to the data analysis from Analytical and Testing Center, Northeastern University.

Appendix A. Supplementary data

Supplementary data to this article can be found online at <https://doi.org/10.1016/j.jechem.2020.08.005>.

References

- [1] V. Augustyn, J. Come, M.A. Lowe, J.W. Kim, P.-L. Taberna, S.H. Tolbert, H.D. Abruña, P. Simon, B. Dunn, *Nat. Mater.* 12 (2013) 518–522.
- [2] M. Mao, X. Wu, Y. Hu, Q. Yuan, Y.-B. He, F. Kang, *J. Energy Chem.* 52 (2021) 277–283.
- [3] Z. Huang, A. Chen, F. Mo, G. Liang, X. Li, Q. Yang, Y. Guo, Z. Chen, Q. Li, B. Dong, C. Zhi, *Adv. Energy Mater.* 10 (2020) 2001024.
- [4] Y. Zhang, F. Wan, S. Huang, S. Wang, Z. Niu, J. Chen, *Nat. Commun.* 11 (2020) 1–10.
- [5] G.G. Yadav, D. Turney, J. Huang, X. Wei, S. Banerjee, *ACS Energy Lett.* 4 (2019) 2144–2146.
- [6] G. Fang, S. Liang, Z. Chen, P. Cui, X. Zheng, A. Pan, B. Lu, X. Lu, J. Zhou, *Adv. Funct. Mater.* 29 (2019) 1905267.
- [7] T. Zhang, Y. Tang, G. Fang, C. Zhang, H. Zhang, X. Guo, X. Cao, J. Zhou, A. Pan, S. Liang, *Adv. Funct. Mater.* (2020) 2002711.
- [8] D. Chen, M. Lu, D. Cai, H. Yang, W. Han, *J. Energy Chem.* 54 (2021) 712–726.
- [9] W. Xu, Y. Wang, *Nano-Micro Lett.* 11 (2019) 90.
- [10] T. Xue, H.J. Fan, *J. Energy Chem.* 54 (2021) 194–201.
- [11] B. She, L. Shan, H. Chen, J. Zhou, X. Guo, G. Fang, X. Cao, S. Liang, *J. Energy Chem.* 37 (2019) 172–175.
- [12] Q. Yang, Y. Guo, B. Yan, C. Wang, Z. Liu, Z. Huang, Y. Wang, Y. Li, H. Li, L. Song, J. Fan, C. Zhi, *Adv. Mater.* 32 (2020) 2001755.
- [13] G. Fang, J. Zhou, A. Pan, S. Liang, *ACS Energy Lett.* 3 (2018) 2480–2501.
- [14] Y. Tang, X. Li, H. Lv, D. Xie, W. Wang, C. Zhi, H. Li, *Adv. Energy Mater.* (2020) 2000892.
- [15] X. Wang, S. Zheng, F. Zhou, J. Qin, X. Shi, S. Wang, C. Sun, X. Bao, Z.-S. Wu, *Nat. Sci. Rev.* 7 (2020) 64–72.
- [16] X. Wang, Y. Li, S. Wang, F. Zhou, P. Das, C. Sun, S. Zheng, Z.-S. Wu, *Adv. Energy Mater.* 10 (2020) 2000081.
- [17] Y. Ma, H. Chang, M. Zhang, Y. Chen, *Adv. Mater.* 27 (2015) 5296–5308.
- [18] S. Chen, L. Ma, K. Zhang, M. Kamruzzaman, C. Zhi, J.A. Zapien, *J. Mater. Chem. A* 7 (2019) 7784–7790.
- [19] L. Dong, X. Ma, Y. Li, L. Zhao, W. Liu, J. Cheng, C. Xu, B. Li, Q.-H. Yang, F. Kang, *Energy Storage Mater.* 13 (2018) 96–102.
- [20] S. Wu, Y. Chen, T. Jiao, J. Zhou, J. Cheng, B. Liu, S. Yang, K. Zhang, W. Zhang, *Adv. Energy Mater.* 9 (2019) 1902915.
- [21] P. Liu, W. Liu, Y. Huang, P. Li, J. Yan, K. Liu, *Energy Storage Mater.* 25 (2020) 858–865.
- [22] H. Zhang, Q. Liu, Y. Fang, C. Teng, X. Liu, P. Fang, Y. Tong, X. Lu, *Adv. Mater.* 31 (2019) 1904948.
- [23] Y. Lu, Z. Li, Z. Bai, H. Mi, C. Ji, H. Pang, C. Yu, J. Qiu, *Nano Energy* 66 (2019) 104132.
- [24] Y. Dong, M. Yu, Z. Wang, T. Zhou, Y. Liu, X. Wang, Z. Zhao, J. Qiu, *Energy Storage Mater.* 7 (2017) 181–188.
- [25] Y. Dong, W. Shi, P. Lu, J. Qin, S. Zheng, B. Zhang, X. Bao, Z.-S. Wu, *J. Mater. Chem. A* 6 (2018) 14324–14329.
- [26] Q. Yang, Z. Huang, X. Li, Z. Liu, H. Li, G. Liang, D. Wang, Q. Huang, S. Zhang, S. Chen, C. Zhi, *ACS Nano* 13 (2019) 8275–8283.
- [27] M. Li, J. Meng, Q. Li, M. Huang, X. Liu, K.A. Owusu, Z. Liu, L. Mai, *Adv. Funct. Mater.* 28 (2018) 1802016.
- [28] R. Chen, J. Yao, Q. Gu, S. Smeets, C. Baerlocher, H. Gu, D. Zhu, W. Morris, O.M. Yaghi, H. Wang, *Chem. Commun.* 49 (2013) 9500–9502.
- [29] G. Fang, Q. Wang, J. Zhou, Y. Lei, Z. Chen, Z. Wang, A. Pan, S. Liang, *ACS Nano* 13 (2019) 5635–5645.
- [30] G. Fang, Z. Wu, J. Zhou, C. Zhu, X. Cao, T. Lin, Y. Chen, C. Wang, A. Pan, S. Liang, *Adv. Energy Mater.* 8 (2018) 1703155.
- [31] F. Zheng, Y. Yang, Q. Chen, *Nat. Commun.* 5 (2014) 5261.
- [32] H. Yang, X. Wang, *Adv. Mater.* 31 (2018) 1800743.
- [33] D. Liu, M. Li, X. Li, F. Ren, P. Sun, L. Zhou, *Chem. Eng. J.* 387 (2020) 124008.
- [34] P. Zhang, F. Sun, Z. Xiang, Z. Shen, J. Yun, D. Cao, *Energy Environ. Sci.* 7 (2014) 442–450.
- [35] B.Y. Xia, Y. Yan, N. Li, H.B. Wu, X.W. Lou, X. Wang, *Nat. Energy* 1 (2016) 15006.
- [36] W. Zhang, J. Yin, M. Sun, W. Wang, C. Chen, M. Altunkaya, A.H. Emwas, Y. Han, U. Schwingenschlogl, H.N. Alshareef, *Adv. Mater.* 32 (2020) 2000732.
- [37] J. Liu, Y. Zhang, L. Zhang, F. Xie, A. Vasileff, S.Z. Qiao, *Adv. Mater.* 31 (2019) 1901261.
- [38] Y. Liu, X. Chen, Y. Yang, Y. Feng, D. Wu, S. Mao, *Chem. Eng. J.* 358 (2019) 408–418.
- [39] Y.-Z. Chen, C. Wang, Z.-Y. Wu, Y. Xiong, Q. Xu, S.-H. Yu, H.-L. Jiang, *Adv. Mater.* 27 (2015) 5010–5016.
- [40] F. Wei, X. He, L. Ma, H. Zhang, N. Xiao, J. Qiu, *Nano-Micro Lett.* 12 (2020) 1–12.
- [41] S. Fleischmann, J.B. Mitchell, R. Wang, C. Zhan, D.E. Jiang, V. Presser, V. Augustyn, *Chem. Rev.* 120 (2020) 6738–6782.
- [42] Z. Li, D. Chen, Y. An, C. Chen, L. Wu, Z. Chen, Y. Sun, X. Zhang, *Energy Storage Mater.* 28 (2020) 307–314.
- [43] Z. Wang, J. Huang, Z. Guo, X. Dong, Y. Liu, Y. Wang, Y. Xia, *Joule* 3 (2019) 1289–1300.
- [44] Z. Pan, Z. Lu, L. Xu, D. Wang, *Appl. Surf. Sci.* 510 (2020) 145384.
- [45] Y. Dong, Y. Li, H. Shi, J. Qin, S. Zheng, R. He, Z.-S. Wu, *Carbon* 159 (2020) 213–220.
- [46] X. Yang, A.L. Rogach, *Adv. Energy Mater.* 9 (2019) 1900747.
- [47] B. Jia, W. Chen, J. Luo, Z. Yang, L. Li, L. Guo, *Adv. Mater.* 32 (2020) 1906582.
- [48] D. Tang, X. Sun, D. Zhao, J. Zhu, W. Zhang, X. Xu, Z. Zhao, *ChemCatChem* 10 (2018) 1291–1299.
- [49] L. Dong, W. Yang, W. Yang, C. Wang, Y. Li, C. Xu, S. Wan, F. He, F. Kang, G. Wang, *Nano-Micro Lett.* 11 (2019) 94.
- [50] Q. Wang, S. Wang, X. Guo, L. Ruan, N. Wei, Y. Ma, J. Li, M. Wang, W. Li, W. Zeng, *Adv. Electron. Mater.* 5 (2019) 1900537.